Role of localized electronic states in high-order harmonic generation from doped semiconductors

Yuntian Zhang [1], Wei He,[1] Liang Li,[1,*] Hubin Cui,[1] Sen Qiao,[1] Pengfei Lan,[1,†] and Peixiang Lu [1,2,3]

[1]*School of Physics and Wuhan National Laboratory for Optoelectronics, Huazhong University of Science and Technology, Wuhan 430074, China*

[2]*Hubei Key Laboratory of Optical Information and Pattern Recognition, Wuhan Institute of Technology, Wuhan 430205, China*

[3]*CAS Center for Excellence in Ultra-intense Laser Science, Shanghai 201800, China*

We investigate high-order harmonic generation (HHG) in sparsely doped semiconductors. The doping in semiconductors breaks the periodic translation invariance in space and introduces localized electronic states (LESs), which leads to two additional electron transition channels, namely, the nonvertical transitions and transitions from LESs. By involving these channels, one can intuitively understand the enhancement of the harmonic yield and the extension of the cutoff energy found in previous works. Moreover, the transition from LESs is space localized and shows self-probed behavior under strong laser fields, encoding the structure information into the HHG. To demonstrate this, we analyze the HHG process in a doped semiconductor with a pair of impurities, where the recombination process of the electron from LESs can be interpreted as a two-center interference. This imprints the internuclear separation between the impurities into the minima of the harmonic spectra. Our work reveals the underlying physical mechanisms in HHG from doped semiconductors and suggests all-optical metrology for structural and dynamic information of LESs.

I. INTRODUCTION

High-order harmonic generation (HHG) is a fascinating strong-field phenomenon in laser-matter interaction which can be used to generate coherent extreme-ultraviolet light sources [1,2] and builds the foundation of attosecond science [3–6]. In recent years, the observation of HHG from solids [7] has opened up new avenues for probing the ultrafast dynamics in condensed matter. By studying the mechanism of HHG [8–15], it is now possible to detect the optoelectronic properties of semiconductors, such as the band structure [16–18], transition dipole moment [19–22], and spatial arrangement of atoms [23–25].

Doped semiconductors form the basis of most modern semiconductor devices and are of particular interest since impurities and defects are inevitable in actual crystals [26]. Recently, HHG from a doped semiconductor was also investigated, and an enhanced harmonic yield by 1–3 orders of magnitude was shown with a periodic doped semiconductor [27]. Subsequent research focused on the harmonic yields [28–30], revealing the effect of doping on the harmonic enhancement and cutoff extension [31–36]. Besides the control of HHG, it is promising to extend well-established techniques from strong-field physics in gases to doped semiconductors [37,38]. This allows us to investigate the doping effect at the electron scale and thus contribute to the development of the next generation of optoelectronic devices. To this end, one needs to accurately understand the effect of

doping on semiconductor properties and their role in HHG processes. According to the standard description of doped semiconductors [26], a trace amount of doping can significantly modulate the properties of semiconductors. The doping breaks the period translation invariance in space, leading to the emergence of localized electronic states (LESs). Interaction between the LESs and Bloch electrons determines the properties of the doped semiconductors and thus is crucial for understanding the HHG process. However, previous studies mainly focused on the influence of doping on the band structure and electron population. An analytical theoretical framework for understanding the underlying physical mechanisms in HHG from doped semiconductors remains to be elucidated.

In this work, we provide an analytical theoretical framework for HHG in sparsely doped semiconductors. Our theory indicates that doping introduces the LESs and perturbs the Bloch states in intrinsic semiconductors, which affects the transition process among these states. Beyond the vertical transitions (VTs) in the present three-step model [39,40], transitions to states with various crystal momenta are introduced, i.e., the nonvertical transition (NT) and the transition from LESs. These additional transition mechanisms allow more electrons to excite into the conduction bands (CBs) and participate in the HHG process. This leads to the enhancement of the harmonics.

Furthermore, the LES is distributed at the location of the impurities, and the transition from LESs can directly link to the spatial arrangement of the impurities. To demonstrate this, we further investigate the HHG process in a donor-doped semiconductor with a pair of impurities. We connect the harmonic spectra and the LES by analyzing the transition dipole

*liangl@hust.edu.cn
†pengfeilan@hust.edu.cn

moment (TDM). Our analysis indicates a two-center interference phenomenon stemming from the transition from the LES. This two-center interference has the potential to extract the internuclear separation between the impurities from the positions of the minima in harmonic spectra. Our work paves the way for studying impurities in materials using the available techniques from strong-field physics and offers insight into the HHG process in doped semiconductors.

II. SOLVING THE TIME-DEPENDENT SCHRÖDINGER EQUATION

In this work, we numerically simulate the HHG in doped semiconductors by solving the time-dependent Schrödinger equation (TDSE). In the length gauge, the time-dependent Hamiltonian is

$$\hat{H}(t) = \hat{H}_0 + \hat{\boldsymbol{r}} \cdot \boldsymbol{F}(t). \tag{1}$$

Unless otherwise indicated, atomic units are used throughout. Here $\boldsymbol{F}(t)$ is the electric field of the laser, $\hat{H}_0 = \hat{\boldsymbol{p}}^2/2 + U(\boldsymbol{r})$ is the field-free Hamiltonian, and $\hat{\boldsymbol{p}}$ is the momentum operator. The potential $U(\boldsymbol{r})$ in doped semiconductors is

$$U(\boldsymbol{r}) = U_0(\boldsymbol{r}) + U'(\boldsymbol{r}). \tag{2}$$

Here $U_0(\boldsymbol{r})$ is the periodic potential of the perfect crystal, and $U'(\boldsymbol{r})$ is the additional potential introduced by doped impurities. We solve the eigenvalue equation of $\hat{H}_0$,

$$\hat{H}_0|\phi_j\rangle = E_j|\phi_j\rangle, \tag{3}$$

to obtain the eigenstates $|\phi_j\rangle$ and the eigenenergies E_j. $|\phi_0\rangle$ stands for the LES, and E_0 is the energy of the LES. The finite-difference method is used in real space; the nonzero matrix elements $H_{l,l'}$ of the operator $\hat{H}_0$ are

$$H_{l,l} = \frac{1}{(dx)^2} + \frac{1}{(dy)^2} + U_l,$$

$$H_{l,l-Ny} = H_{l,l+Ny} = -\frac{1}{2(dx)^2},$$

$$H_{l,l-1} = H_{l,l+1} = -\frac{1}{2(dy)^2}. \tag{4}$$

Here dx and dy are the grid spacings, $l = (nx-1)Ny + ny$ is the number of two-dimensional grid points, and nx (ny) is the number of grid points in the x (y) direction. Ny is the total number of grid points in the y direction. With the eigenstates $|\phi_j\rangle$ being the initial states, the TDSE

$$\hat{H}(t)|\Psi(t)\rangle = i\frac{\partial}{\partial t}|\Psi(t)\rangle \tag{5}$$

is solved using the split-operator method [41] to obtain the time evolution of the system. To avoid unphysical reflections of the wave function at the edges of the grid, an absorbing boundary is used. The laser-induced current can be calculated as

$$\boldsymbol{J}(t) = -\frac{d}{dt}\langle\Psi(t)|\hat{\boldsymbol{r}}|\Psi(t)\rangle. \tag{6}$$

The harmonic spectrum is obtained by calculating the Fourier transform of the laser-induced current

$$I(\omega) \propto |\mathcal{FT}[\boldsymbol{J}(t)]|^2. \tag{7}$$

III. ROLE OF LOCALIZED ELECTRONIC STATES

According to the Noether theorems [42], an invariance corresponds to a conservation law. Especially, periodic translation invariance corresponds to the conservation of momentum. For that reason, in a perfect crystal with periodic translation invariance, the transition of the electrons can occur only between states with the same crystal momentum. But in a doped semiconductor, the doped impurities break the periodic translation invariance, and the crystal momentum is no longer conserved in the transition process. The goal of this section is to establish an analytical theoretical framework and demonstrate the underlying physical mechanisms for the HHG process in doped semiconductors.

We start with Eqs. (1), (2), and (5). In an intrinsic semiconductor, the additional potential $U'(\boldsymbol{r}) = 0$, and the eigenstates of $\hat{H}_0$ satisfy the Bloch theorem and Born–von Kármán periodic boundary conditions [43], so $\Psi(t)$ can be written as

$$|\Psi(t)\rangle = \sum_{n,\boldsymbol{k}} a_{n,\boldsymbol{k}}(t)|\phi_{n,\boldsymbol{k}}\rangle, \tag{8}$$

$$\langle\boldsymbol{r}|\phi_{n,\boldsymbol{k}}\rangle = u_{n,\boldsymbol{k}}(\boldsymbol{r})\, e^{i\boldsymbol{k}\cdot\boldsymbol{r}}. \tag{9}$$

Here $|\phi_{n,\boldsymbol{k}}\rangle$ are the Bloch states and eigenstates of $\hat{H}_0$. $u_{n,\boldsymbol{k}}(\boldsymbol{r})$ are the periodic part of the Bloch states, $a_{n,\boldsymbol{k}}(t)$ are the probability amplitude, n is the band index, and $\boldsymbol{k}$ is the crystal momentum.

In a doped semiconductor, the additional potential $U'(\boldsymbol{r})$ is introduced. Consider the case of sparsely doped semiconductors; the additional potential is localized and distributes only near the impurities. So $U'(\boldsymbol{r})$ can be treated as a perturbation. By using perturbation theory, the eigenstates of $\hat{H}_0$ can be written as

$$|\phi'_{n,\boldsymbol{k}}\rangle = |\phi_{n,\boldsymbol{k}}\rangle + |\Delta\phi_{n,\boldsymbol{k}}\rangle, \tag{10}$$

$$|\Delta\phi_{n,\boldsymbol{k}}\rangle = \sum_{n_1,\boldsymbol{k_1}} C^{n,\boldsymbol{k}}_{n_1,\boldsymbol{k_1}}|\phi_{n_1,\boldsymbol{k_1}}\rangle. \tag{11}$$

Here $C^{n,\boldsymbol{k}}_{n_1,\boldsymbol{k_1}}$ can be obtained using the time-independent degenerate perturbation theory [44]. Note that the normalization is performed so that $\langle\phi'_{n,\boldsymbol{k}}|\phi'_{n,\boldsymbol{k}}\rangle = 1$. In addition, the LES $|\phi_0\rangle$ is introduced in the doped semiconductor. So $\Psi(t)$ can be written as

$$|\Psi(t)\rangle = a_0(t)|\phi_0\rangle + \sum_{n,\boldsymbol{k}} a_{n,\boldsymbol{k}}(t)|\phi'_{n,\boldsymbol{k}}\rangle. \tag{12}$$

We defined $a_{n,\boldsymbol{k_0}}(t) = b_{n,\boldsymbol{k_0}}(t)e^{-i\int_{t_0}^{t} E_n(\boldsymbol{k}(\tau))d\tau}$ and $a_0(t) = b_0(t)e^{-i\int_{t_0}^{t} E_0 d\tau}$. The transformation $\boldsymbol{k} = \boldsymbol{k_0} + \boldsymbol{A}(t)$ is used, $\boldsymbol{k_0}$ is the crystal momentum at initial time t_0, and $\boldsymbol{A}(t) = -\int_{t_0}^{t} \boldsymbol{F}(\tau)d\tau$ is the vector potential of the laser field. We insert Eq. (12) into the TDSE [Eq. (5)], $\langle\phi'_{m,\boldsymbol{k'}}|$ is multiplied by the equation, and the orthonormality relationship is used; then we obtain

$$\frac{\partial b_{m,\boldsymbol{k_0}'}(t)}{\partial t} = -i\sum_{n,\boldsymbol{k}} b_{n,\boldsymbol{k_0}}(t)\boldsymbol{F}(t) \cdot \boldsymbol{d}'_{mn}(\boldsymbol{k'},\boldsymbol{k})e^{i\int_{t_0}^{t} E_m(\boldsymbol{k'})-E_n(\boldsymbol{k})d\tau}$$

$$- ib_0(t)\boldsymbol{F}(t) \cdot \boldsymbol{d}_{m0}(\boldsymbol{k'})\, e^{i\int_{t_0}^{t} E_m(\boldsymbol{k'})-E_0 d\tau}. \tag{13}$$

Here $E_n(\boldsymbol{k})$ is the band structure, and the integration in the exponentiation is the dynamical phase accumulated during the

evolution. Equation (13) elucidates the transition process of the electrons among the states in the energy bands and the LES.

(1) $\boldsymbol{F}(t) \cdot \boldsymbol{d}'_{mn}(\boldsymbol{k}', \boldsymbol{k})$ in the first row of Eq. (13) stands for the transition between bands m and n. The TDM $\boldsymbol{d}'_{mn}(\boldsymbol{k}', \boldsymbol{k})$ is defined as

$$
\begin{aligned}
\boldsymbol{d}'_{mn}(\boldsymbol{k}', \boldsymbol{k}) &= \langle \phi'_{m,\boldsymbol{k}'} | \boldsymbol{r} | \phi'_{n,\boldsymbol{k}} \rangle + i\delta_{\boldsymbol{k}'\boldsymbol{k}}\delta_{mn}\nabla_{\boldsymbol{k}} \\
&= \langle \phi_{m,\boldsymbol{k}'} | \boldsymbol{r} | \phi_{n,\boldsymbol{k}} \rangle + i\delta_{\boldsymbol{k}'\boldsymbol{k}}\delta_{mn}\nabla_{\boldsymbol{k}} \\
&\quad + \langle \Delta\phi_{m,\boldsymbol{k}'} | \boldsymbol{r} | \phi_{n,\boldsymbol{k}} \rangle + \langle \phi_{m,\boldsymbol{k}'} | \boldsymbol{r} | \Delta\phi_{n,\boldsymbol{k}} \rangle \\
&\quad + \langle \Delta\phi_{m,\boldsymbol{k}'} | \boldsymbol{r} | \Delta\phi_{n,\boldsymbol{k}} \rangle.
\end{aligned} \tag{14}
$$

Using Eqs. (9) and (11) and the relation

$$
\langle \phi_{m,\boldsymbol{k}'} | \boldsymbol{r} | \phi_{n,\boldsymbol{k}} \rangle = -i\delta_{\boldsymbol{k}'\boldsymbol{k}}\delta_{mn}\nabla_{\boldsymbol{k}} + i\delta_{\boldsymbol{k}'\boldsymbol{k}}\int_{\text{cell}} u^*_{m\boldsymbol{k}'}(\boldsymbol{r})\nabla_{\boldsymbol{k}}u_{n\boldsymbol{k}}(\boldsymbol{r})d\boldsymbol{r}, \tag{15}
$$

Eq. (14) becomes

$$
\boldsymbol{d}'_{mn}(\boldsymbol{k}', \boldsymbol{k}) = \delta_{\boldsymbol{k}'\boldsymbol{k}}\boldsymbol{d}_{mn}(\boldsymbol{k}') + \boldsymbol{\Delta d}_{mn}(\boldsymbol{k}', \boldsymbol{k}). \tag{16}
$$

Here $\boldsymbol{d}_{mn}(\boldsymbol{k}') = i\int_{\text{cell}} u^*_{m\boldsymbol{k}'}(\boldsymbol{r})\nabla_{\boldsymbol{k}}u_{n\boldsymbol{k}}(\boldsymbol{r})d\boldsymbol{r}$ is the common TDM. $\delta_{\boldsymbol{k}'\boldsymbol{k}}$ tells us the transition can happen only between the states with the same crystal momentum. So we call $\boldsymbol{F}(t) \cdot \boldsymbol{d}_{mn}(\boldsymbol{k}')$ the VT term.

(2) Using Eq. (11) and the definition of the common TDM $\boldsymbol{d}_{mn}(\boldsymbol{k}')$, $\boldsymbol{\Delta d}_{mn}(\boldsymbol{k}', \boldsymbol{k})$ can be written as the linear combination of $\boldsymbol{d}_{mn}(\boldsymbol{k}')$,

$$
\begin{aligned}
\boldsymbol{\Delta d}_{mn}(\boldsymbol{k}', \boldsymbol{k}) &= \sum_{n_1} \left(C^{m,\boldsymbol{k}'}_{n_1,\boldsymbol{k}}\right)^* \boldsymbol{d}_{n_1 n}(\boldsymbol{k}) \\
&\quad + \sum_{n_2} C^{n,\boldsymbol{k}}_{n_2,\boldsymbol{k}'} \boldsymbol{d}_{mn_2}(\boldsymbol{k}') \\
&\quad + \sum_{n_1 n_2 \boldsymbol{k_1}} \left(C^{m,\boldsymbol{k}'}_{n_1,\boldsymbol{k_1}}\right)^* C^{n,\boldsymbol{k}}_{n_2,\boldsymbol{k_1}} \boldsymbol{d}_{n_1 n_2}(\boldsymbol{k_1}),
\end{aligned} \tag{17}
$$

which is the result of the lack of periodic translation invariance. Equation (17) indicates the additional transition channels between various $\boldsymbol{k}$ and $\boldsymbol{k}'$. So we call $\boldsymbol{F}(t) \cdot \boldsymbol{\Delta d}_{mn}(\boldsymbol{k}', \boldsymbol{k})$ the NT term.

(3) $\boldsymbol{F}(t) \cdot \boldsymbol{d}_{m0}(\boldsymbol{k}')$ in the second row of Eq. (13) stands for the transition between band m and the LES. The TDM $\boldsymbol{d}_{m0}(\boldsymbol{k}')$ is defined as

$$
\boldsymbol{d}_{m0}(\boldsymbol{k}') = \langle \phi'_{m,\boldsymbol{k}'} | \boldsymbol{r} | \phi_0 \rangle \approx \langle \phi_{m,\boldsymbol{k}'} | \boldsymbol{r} | \phi_0 \rangle. \tag{18}
$$

The assumption $|\phi'_{m,\boldsymbol{k}'}\rangle \approx |\phi_{m,\boldsymbol{k}'}\rangle$ is used. $\boldsymbol{d}_{m0}(\boldsymbol{k}')$ indicates the additional transition channels introduced by the LES. Equation (18) means that the transition can take place between $|\phi_0\rangle$ and all the other states with various crystal momenta $\boldsymbol{k}'$ in band m. So we call $\boldsymbol{F}(t) \cdot \boldsymbol{d}_{m0}(\boldsymbol{k}')$ the localized electronic state transition (LEST) term. Note that the gauge transformation is performed to deal with the random phase of the TDM in this work [45].

The contributions of the VT, NT, and LEST channels can be separated by classifying the laser-induced current. The laser-induced current can be calculated as $\boldsymbol{J}(t) = -\langle \Psi(t) | \hat{\boldsymbol{p}} | \Psi(t) \rangle$. By using Eq. (12), the current $\boldsymbol{J}(t)$ can be separated into the contributions of the VT, NT, and LEST:

$$
\begin{aligned}
\boldsymbol{J}_{\text{VT}}(t) &= -\sum_{m \neq n, \boldsymbol{k}=\boldsymbol{k}'} b^*_{m\boldsymbol{k}_0}(t)b_{n\boldsymbol{k}_0}(t)e^{i\int_{t_0}^{t} E_m(\boldsymbol{k}')-E_n(\boldsymbol{k})d\tau}, \\
&\quad \times \langle \phi'_{m\boldsymbol{k}'} | \hat{\boldsymbol{p}} | \phi'_{n\boldsymbol{k}} \rangle \\
\boldsymbol{J}_{\text{NT}}(t) &= -\sum_{m \neq n, \boldsymbol{k} \neq \boldsymbol{k}'} b^*_{m\boldsymbol{k}_0}(t)b_{n\boldsymbol{k}_0}(t)e^{i\int_{t_0}^{t} E_m(\boldsymbol{k}')-E_n(\boldsymbol{k})d\tau}, \\
&\quad \times \langle \phi'_{m\boldsymbol{k}'} | \hat{\boldsymbol{p}} | \phi'_{n\boldsymbol{k}} \rangle \\
\boldsymbol{J}_{\text{LEST}}(t) &= -\sum_{m, \boldsymbol{k}'} b^*_{m\boldsymbol{k}_0}(t)b_0(t)e^{i\int_{t_0}^{t} E_m(\boldsymbol{k}')-E_0 d\tau} \\
&\quad \times \langle \phi'_{m\boldsymbol{k}'} | \hat{\boldsymbol{p}} | \phi_0 \rangle + \text{c.c.}
\end{aligned} \tag{19}
$$

The summations run over all $\boldsymbol{k} = \boldsymbol{k}'$ for the VT and $\boldsymbol{k} \neq \boldsymbol{k}'$ for the NT. Here $\langle \phi'_{m\boldsymbol{k}'} | \hat{\boldsymbol{p}} | \phi'_{n\boldsymbol{k}} \rangle = i[E_m(\boldsymbol{k}') - E_n(\boldsymbol{k})]\boldsymbol{d}'_{mn}(\boldsymbol{k}', \boldsymbol{k})$, and $\langle \phi'_{m\boldsymbol{k}'} | \hat{\boldsymbol{p}} | \phi_0 \rangle = i[E_m(\boldsymbol{k}') - E_0]\boldsymbol{d}_{m0}(\boldsymbol{k}')$. The corresponding harmonic intensity can be obtained by calculating the Fourier transform of the currents

$$
\begin{aligned}
\boldsymbol{I}_{\text{VT}}(\omega) &\propto |\mathcal{FT}[\boldsymbol{J}_{\text{VT}}(t)]|^2, \\
\boldsymbol{I}_{\text{NT}}(\omega) &\propto |\mathcal{FT}[\boldsymbol{J}_{\text{NT}}(t)]|^2, \\
\boldsymbol{I}_{\text{LEST}}(\omega) &\propto |\mathcal{FT}[\boldsymbol{J}_{\text{LEST}}(t)]|^2.
\end{aligned} \tag{20}
$$

The above method provides an analytical theoretical framework for understanding the HHG process in sparsely doped semiconductors. The theoretical framework can be widely used for different kinds of imperfect crystals, including, but not limited to, the cases of vacancy defect, shallow impurities, deep impurities, acceptor doping, and donor doping. To demonstrate the effect of the VT, NT, and LEST channels, we consider the HHG process in a donor-doped semiconductor as an example. Our model is based on a linear chain of N atoms located with a separation a_0. A widely used Mathieu-type potential [46] is used as the periodic potential of the intrinsic semiconductor, which is written as

$$
U_0(x) = -v_0[1 + \cos(2\pi x/a_0)]. \tag{21}
$$

Here we choose $v_0 = 0.37$ a.u., $a_0 = 8$ a.u., and $N = 200$. We consider the case in which the atom located at $x = 0$ is replaced by the impurity atom. Therefore, the potential of the doped semiconductor is written as

$$
U(x) = \begin{cases} -v_1[1 + \cos(2\pi x/a_0)] & |x| \leqslant a_0/2, \\ -v_0[1 + \cos(2\pi x/a_0)] & |x| > a_0/2. \end{cases} \tag{22}
$$

We use $v_1 = 0.62$ a.u. to model the donor-doped semiconductor.

The band structure of the semiconductors is shown in Fig. 1, where we show only the valence band (VB), the first CB (CB1), and the second CB (CB2). We can see that the band structure of the donor-doped semiconductor in Fig. 1(b) is almost the same as that of the intrinsic semiconductor in Fig. 1(a), except for the energy levels of the LES that appear in the band gap between CB1 and the VB. We analyze the transition process by using Eq. (13). The VT, NT, and LEST channels are indicated by the arrows in Fig. 1. As we can see, there are only VT channels between the states with the same k (blue arrows) in the intrinsic semiconductor. The doping
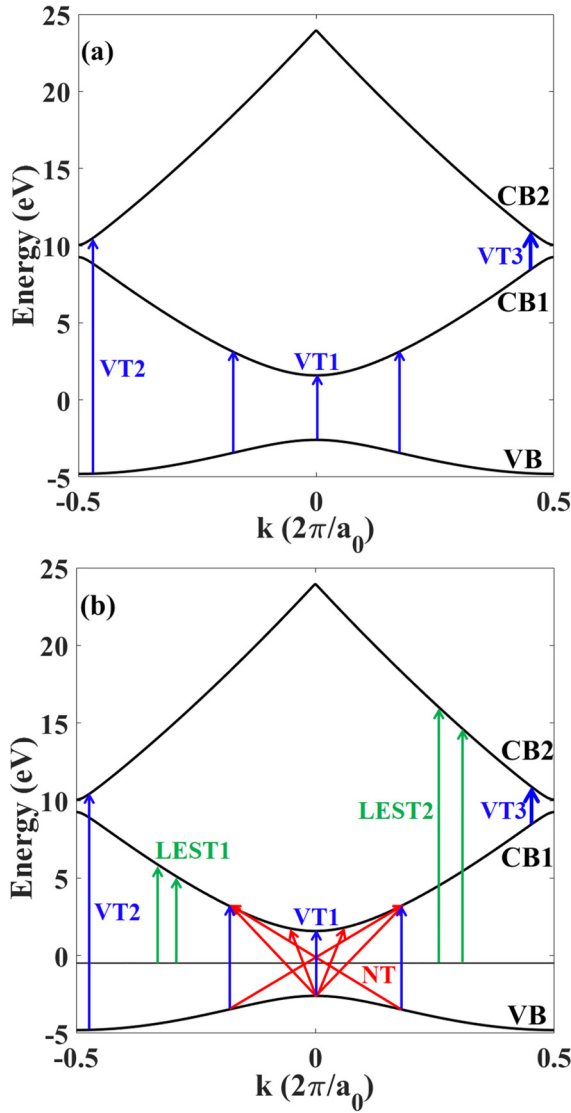
FIG. 1. The band structure of (a) the intrinsic semiconductor and (b) donor-doped semiconductor. The horizontal line in (b) indicates the energy of the LES. The VT, NT, and LEST channels are indicated by the blue, red, and green arrows, respectively. The VT channels between VB and CB1 (CB2) are labeled VT1 (VT2). The VT channels between CB1 and CB2 are labeled VT3. The LEST channels between the LES and CB1 (CB2) are labeled LEST1 (LEST2).
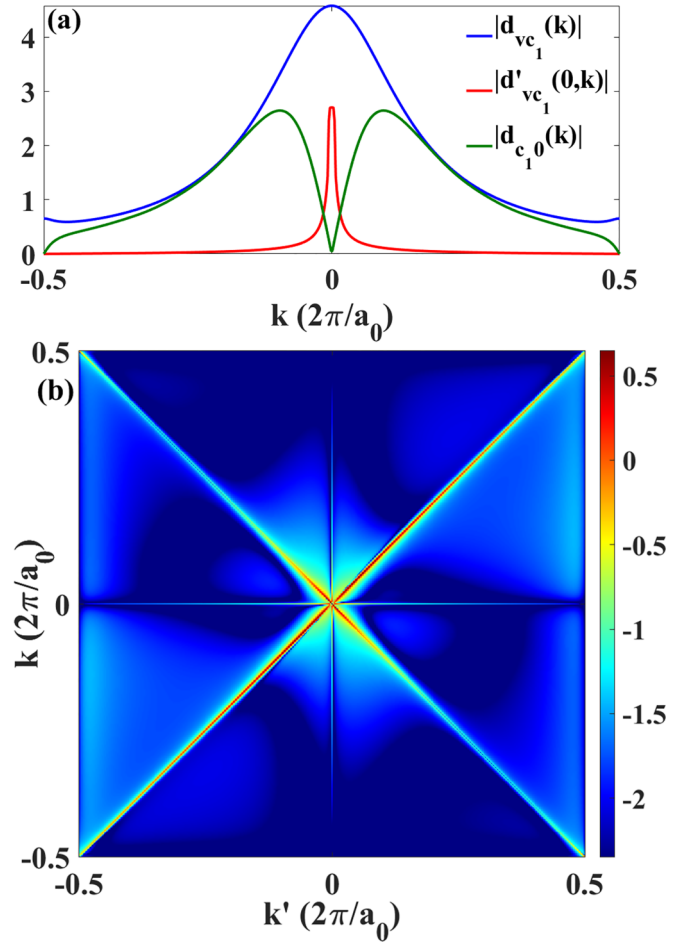

FIG. 2. (a) The TDM for VT1, the NT, and LEST1. The blue curve shows the magnitude of $d_{vc_1}(k)$ for VT1 in the intrinsic semiconductor. In the donor-doped semiconductor, the red curve shows the magnitude of $d'_{vc_1}(k', k)$ from the top of the VB ($k' = 0$) to CB1 states, the green curve shows the magnitude of $d_{c_10}(k)$ for LEST1. (b) The logarithm of the magnitude of the TDM $d'_{vc_1}(k', k)$, i.e., $\log_{10}[|d'_{vc_1}(k', k)|]$, in the donor-doped semiconductor.

breaks the periodic translation invariance, and the NT channels between the states with various k (red arrows) appear. The LES in the donor-doped semiconductor is initially occupied, and the electrons can be excited from the LES through the LEST channels (green arrows). We analyze the transition to CB1 by examining the TDM of the VT1, LEST1, and NT channels. In the intrinsic semiconductor, $d'_{vc_1}(k', k) = \delta_{k'k}d_{vc_1}(k)$. The blue curve in Fig. 2(a) shows the magnitude of $d_{vc_1}(k)$, which corresponds to the common VT1 channels. In the donor-doped semiconductor, the NT channels enable the transition between VB states with k' and CB1 states with k. The red curve in Fig. 2(a) shows the magnitude of $d'_{vc_1}(0, k)$. $d'_{vc_1}(0, k)$ is not equal to zero in a wide range of k, which indicates the electron at the top of the VB ($k' = 0$) can transition

to a large area in CB1. Figure 2(b) shows the logarithm of the magnitude of $d'_{vc_1}(k', k)$. The nonzero antidiagonal line indicates the transition from k to $-k$. This phenomenon is called the backscattering of electrons [30]. The TDM between the LES and CB1 states is shown by the green curve in Fig. 2(a), corresponding to the LEST1 channels. $d_{c_10}(k) \neq 0$ for all k indicate the transition from the LES can reach all the states in CB1. The two maxima of $|d_{c_10}(k)|$ are not at the position of the minimum band gap ($k = 0$). So through the LEST1 channels, the electrons can directly transition to the high-energy states in CB1. The transition process between the other states in the band structure has similar results.

By using Eqs. (13), (19), and (20), we perform a numerical calculation to simulate the HHG process in doped semiconductors. In the calculation, the LES and all the states in the VB are initially occupied. The results are shown in Fig. 3. We compare the contributions of the VT, NT, and LEST. As we can see in Fig. 3, the contribution of the LEST is much bigger than the contributions of the VT and NT. The cutoff energies of the harmonic spectrum contributed by the LEST are 4.8
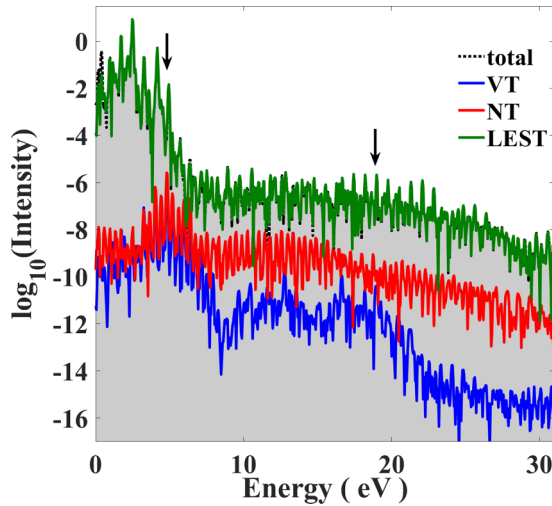
FIG. 3. The harmonic intensity contributed by the VT (blue curve), NT (red curve), and LEST (green curve). The black dotted curve and the gray shaded area indicate the total harmonic intensity. The arrows indicate the cutoff energies at 4.8 and 18.8 eV.
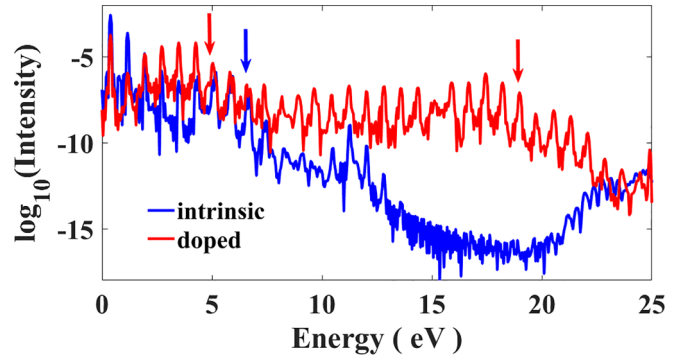

FIG. 4. The harmonic spectra obtained by solving the TDSE. The harmonic spectra for the donor-doped and intrinsic semiconductors are shown. The red and blue arrows indicate the cutoffs of donor-doped and intrinsic harmonic spectra, respectively.

and 18.8 eV, which are consistent with the total harmonic spectrum. Therefore, the LEST dominates the HHG process in the doped semiconductor. In terms of the NT and VT, the NT and VT contribute comparably in the low-energy region, while the contribution of the NT is greater than that of the VT in the high-energy region.

To test our theoretical method and show the effect of the additional transition channels, the harmonic spectra for both intrinsic and donor-doped semiconductors are obtained by solving the TDSE. Since we have proved that the LEST dominates the HHG process, in the rest of this work, the simulations of the HHG process in doped semiconductors are performed with the highest occupied LES being the initial state. For the intrinsic semiconductor, the state at the top of the VB is chosen to be the initial state for comparison. In our calculation, the grid spacing Δx is 0.1 a.u., and the time step Δt is 0.08 a.u. The intensity of the laser pulse is 1×10^{11} W/cm^2, and the wavelength is 3.2 μm. We use a trapezoidal envelope with a total duration of eight optical cycles, including two rising and two falling circles, for all laser pulses in this work. Figure 4 shows the harmonic spectra. We can see the significant enhancement of the harmonics for the donor-doped semiconductor between 7.3 and 23.6 eV compared to the intrinsic case. The harmonic spectrum of the intrinsic semiconductor has a cutoff energy of about 6.5 eV, while the harmonic spectrum of the donor-doped semiconductor has cutoff energies at 4.8 and 18.8 eV, which are indicated by the arrows in Fig. 4.

For further insight into the HHG process, the time-dependent population-imaging (TDPI) method [47] is used. Figure 5 shows the TDPI pictures for both intrinsic and donor-doped semiconductors. In Fig. 5(a), the electron populations of the intrinsic semiconductor oscillate in the VB and CBs, which correspond to the laser-driving Bloch oscillations of electrons in reciprocal space. Because of the VT channels in the intrinsic semiconductor, only a single trajectory can be seen in CB1 and CB2. The red and black dashed lines

indicate the maximum energy and the minimum energy that the electrons can reach in CB1 and the VB, respectively. The maximum energy difference is 6.5 eV, which is consistent with the cutoff of the harmonic spectra for the intrinsic semiconductor in Fig 4. As shown in Fig. 5(b), there are multiple electron trajectories in CB1 and CB2 for the donor-doped semiconductors. This phenomenon corresponds to the NT and LEST channels in the doped semiconductor. It can be seen that the additional transition channels enable more electrons promoted to the CBs and participate in the HHG process, which causes the enhancement of the harmonics. The black dashed line indicates the maximum energy of the main trajectories in CB1. The electron population in the main trajectories is 1–2 orders of magnitude larger than that of the other trajectories in CB1. The energy difference between the black dashed line and the LES is 4.8 eV. This energy difference matches the LEST1 channels in Fig. 1(b) and agrees with the first cutoff of the harmonic spectra for the donor-doped semiconductor in Fig. 4. The red dashed line indicates the maximum energy of the trajectories in CB2. The energy difference between the line and the LES is 18.8 eV, corresponding to the LEST2 channels and the second cutoff of the harmonic spectra for the donor-doped semiconductor. Therefore, the LEST channels are responsible for the enhancement of the harmonic and cutoff change of the harmonic spectra. Similar results can be found in the acceptor-doped semiconductors (see the Appendix).

IV. TWO-CENTER INTERFERENCE

In this section, we focus on the effect of the LEST. The LEST carries information about the spatial distribution of LESs and connects the positions of impurities to the HHG process. To demonstrate this, we consider the HHG process in a donor-doped semiconductor with a pair of impurities. The potential of this semiconductor $U(\boldsymbol{r})$ is the sum of the periodic potential for the perfect crystal

$$U_0(\boldsymbol{r}) = \frac{V_0}{2}\left[\cos\left(\frac{\pi}{a_0}x\right)\right]^2 + \frac{V_0}{2}\left[\cos\left(\frac{\pi}{a_0}y\right)\right]^2 \quad (23)$$
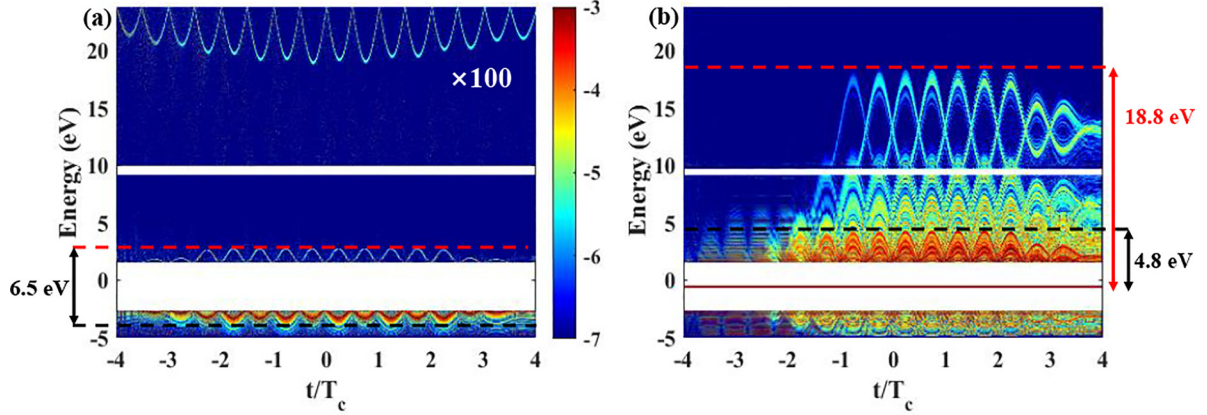
FIG. 5. The TDPI pictures for (a) the intrinsic semiconductor and (b) donor-doped semiconductor. The colors indicate the populations of electrons in the VB, LES, CB1, and CB2. The isolated line between the VB and CB1 in (b) corresponds to the LES. T_c is the optical cycle. For clarity, the electron population in CB2 for the intrinsic semiconductor is multiplied by 100.

and the additional potential introduced by doped impurity

$$U'(\boldsymbol{r}) = -\sum_l \frac{1}{\sqrt{(\boldsymbol{r}-\boldsymbol{r}_l)^2+a^2}} \exp\left(\frac{-|\boldsymbol{r}-\boldsymbol{r}_l|\ln 2}{\sigma}\right). \quad (24)$$

Here $V_0 = -0.9$ a.u., $a_0 = 9$ a.u., $a = 2$ a.u., and $\sigma = a_0/4$. $\boldsymbol{r}_l$ is the position of the impurities, $l = 1, 2$. In Eq. (24), the soft-core potential is used, and the exponential attenuation factor represents the Coulomb shielding effect in solids. The potential $U(\boldsymbol{r})$ is shown in Fig. 6(a). Equations (3) and (4) are solved to obtain the LES $|\phi_0\rangle$ and its energy E_0.
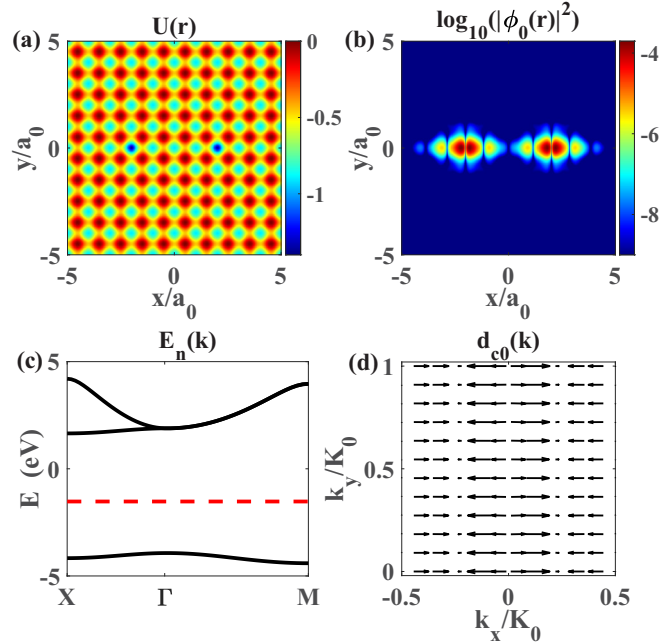

FIG. 6. (a) The potential of the donor-doped semiconductor with a pair of impurities. (b) The logarithm of the electron density distribution in the LES. (c) The band structure of the doped semiconductor. The horizontal dashed line in the band gap indicates the energy of $|\phi_0\rangle$. (d) The TDM for the LEST between $|\phi_0\rangle$ and CB states. The length of the arrows indicates the amplitude of the TDM, and the direction of the arrows indicates the direction of the TDM.

The two-dimensional calculation is performed in the region where $x \in [-15a_0, 15a_0]$ and $y \in [-15a_0, 15a_0]$ with $Nx \times Ny$ points, $Ny = Nx = 3510$, and $dx = dy = 1/13$ a.u. The two-dimensional grids are mapped to one-dimensional grids with $(Nx \times Ny)$ points, so $j \in [1, Nx \times Ny]$ in Eq. (4). The distribution of the LESs is shown in Fig. 6(b). As we can see, $|\phi_0(\boldsymbol{r})|^2$ is localized and mainly distributes near the position of the impurities. So $\phi_0(\boldsymbol{r})$ can be written as

$$\phi_0(\boldsymbol{r}) = \phi_0^1(\boldsymbol{r}) + \phi_0^2(\boldsymbol{r}). \quad (25)$$

$\phi_0^1(\boldsymbol{r})$ and $\phi_0^2(\boldsymbol{r})$ correspond to the part of $\phi_0(\boldsymbol{r})$ localized at each impurity. The energy of $\phi_0(\boldsymbol{r})$ is indicated with a horizontal line in the band gap in Fig. 6(c). The band structure in Fig. 6(c) is calculated based on an empirical pseudopotential Hamiltonian [48]. The TDM for the LEST between the LES and the CB states can be calculated as $\boldsymbol{d}_{c0}(\boldsymbol{k}) = \langle \phi_{ck}|\hat{\boldsymbol{r}}|\phi_0\rangle$; $\boldsymbol{d}_{c0}(\boldsymbol{k})$ is shown in Fig. 6(d). Using Eq. (25) and the Bloch theorem $\phi_{nk}(\boldsymbol{r}) = u_{nk}(\boldsymbol{r})e^{i\boldsymbol{k}\cdot\boldsymbol{r}}$, the TDM $\boldsymbol{d}_{c0}(\boldsymbol{k})$ can be written as

$$\boldsymbol{d}_{c0}(\boldsymbol{k}) = \int u_{ck}^*(\boldsymbol{r})e^{-i\boldsymbol{k}\cdot\boldsymbol{r}}\boldsymbol{r}[\phi_0^1(\boldsymbol{r}) + \phi_0^2(\boldsymbol{r})]\, d\boldsymbol{r}. \quad (26)$$

Because $\phi_0(\boldsymbol{r})$ is highly localized, we can assume $\phi_0^1(\boldsymbol{r}) \approx \phi_0^1(\boldsymbol{r}_1)\delta(\boldsymbol{r}-\boldsymbol{r}_1)$ and $\phi_0^2(\boldsymbol{r}) \approx \phi_0^2(\boldsymbol{r}_2)\delta(\boldsymbol{r}-\boldsymbol{r}_2)$. Equation (26) becomes

$$\boldsymbol{d}_{c0}(\boldsymbol{k}) \approx u_{ck}^*(\boldsymbol{r}_1)e^{-i\boldsymbol{k}\cdot\boldsymbol{r}_1}\boldsymbol{r}_1\phi_0^1(\boldsymbol{r}_1)$$
$$+ u_{ck}^*(\boldsymbol{r}_2)e^{-i\boldsymbol{k}\cdot\boldsymbol{r}_2}\boldsymbol{r}_2\phi_0^2(\boldsymbol{r}_2). \quad (27)$$

Due to the symmetry, one can obtain $\boldsymbol{r}_1 = -\boldsymbol{r}_2$, $u_{ck}^*(\boldsymbol{r}_1) = u_{ck}^*(\boldsymbol{r}_2)$, and $\phi_0^1(\boldsymbol{r}_1) = \pm\phi_0^2(\boldsymbol{r}_2)$. Equation (27) can be written as

$$\boldsymbol{d}_{c0}(\boldsymbol{k}) \approx \boldsymbol{r}_1 u_{ck}^*(\boldsymbol{r}_1)\phi_0^1(\boldsymbol{r}_1)(e^{-i\boldsymbol{k}\cdot\boldsymbol{r}_1} \mp e^{-i\boldsymbol{k}\cdot\boldsymbol{r}_2}). \quad (28)$$

In this section, the highest occupied state in the doped semiconductor is an even-parity LES. We choose the even-parity LES as the initial state, so the interference factor in Eq. (28) becomes $e^{-i\boldsymbol{k}\cdot\boldsymbol{r}_1} - e^{-i\boldsymbol{k}\cdot\boldsymbol{r}_2}$. The odd-parity LESs have similar results (see the Appendix). This interference factor indicates the two-center interference in the LEST process. The two-center interference proposed here is in analogy with
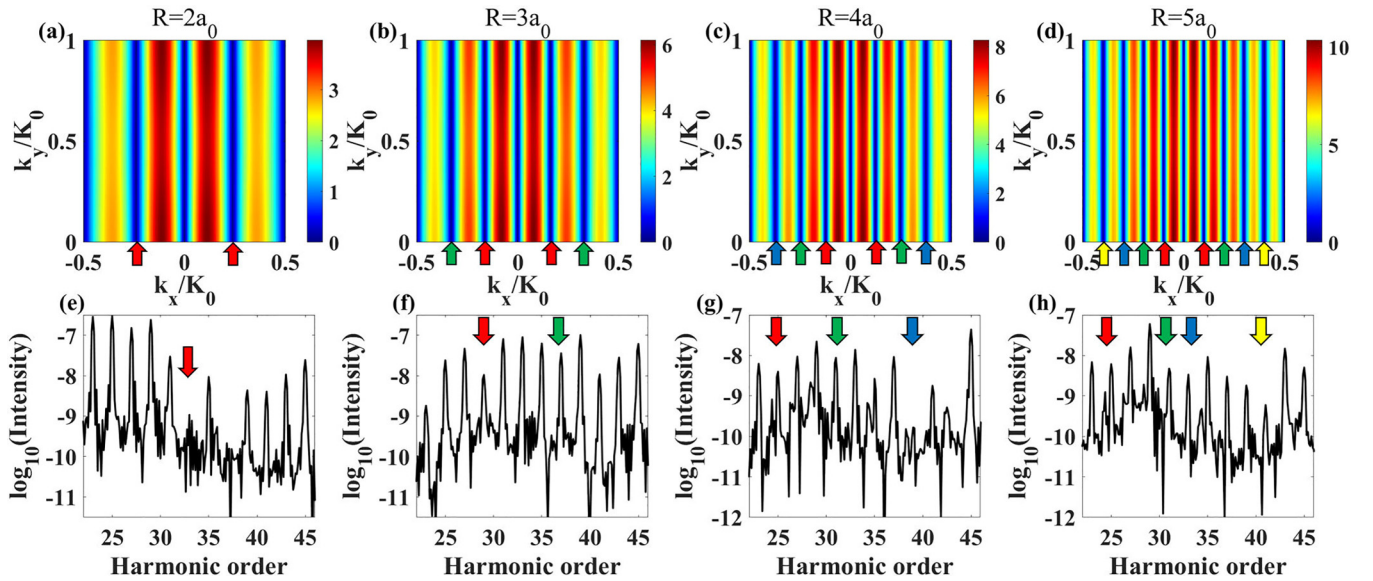
FIG. 7. (a)–(d) show the magnitudes of the TDM $|\boldsymbol{d}_{c0}(\boldsymbol{k})|$ with different internuclear separations: (a) $R = 2a_0$, (b) $R = 3a_0$, (c) $R = 4a_0$, and (d) $R = 5a_0$. (e)–(h) show the parts of harmonic spectra corresponding to the TDM. The arrows indicate the minimums of the harmonic spectra and the corresponding minima of $|\boldsymbol{d}_{c0}(\boldsymbol{k})|$.

the two-center interference in HHG from molecular gases [49–54]. For HHG from solids, a previous study proposed the real-space interference in solids without impurities [15]. In the previous work, the real-space interference was used to test the real-space recollision picture for the HHG process in the intrinsic crystal. However, for doped semiconductors, the two-center interference in the LEST process has not been discussed.

Due to the two-center interference factor in Eq. (28), $\boldsymbol{d}_{c0}(\boldsymbol{k}_r) \approx 0$ when $\boldsymbol{k}_r \cdot (\boldsymbol{r_2} - \boldsymbol{r_1}) = 2m\pi$. m is an integer. The electrons can hardly transition at these crystal momenta $\boldsymbol{k}_r$, and the yield of the harmonics decreases. Therefore, when

$$\boldsymbol{k}_r \cdot R = m\pi, \tag{29}$$

there will be local minima in the harmonic spectra. The relation $|\boldsymbol{r_2} - \boldsymbol{r_1}| = 2R$ is used. The positions of the local minima are at the positions of nth-order harmonics in the harmonic spectra, where

$$n\omega_0 = E_c(\boldsymbol{k}_r) - E_0. \tag{30}$$

Here ω_0 is the photon energy of the driven laser. Note that the positions of the minima are determined in the energy ranges corresponding to the plateau ranges of the harmonic spectra, not in the cutoff ranges of the spectra.

The evolution of this system is simulated by solving the TDSE. We set the initial state $|\Psi(t_0)\rangle = |\phi_0\rangle$, and the time step $\Delta t = 0.1722$ a.u. A driven laser with a wavelength equal to 10 000 nm is used to match the bandwidth of the CB (2.55 eV) and have enough harmonic orders. The intensity of the laser $I_1 = 0.36\,\mathrm{TW/cm^2}$. The intensity of the laser is chosen so that the maximum of $A(t)$ is equal to the width of the first Brillouin zone K_0, i.e., $\max[A(t)] = K_0$. The laser is linearly polarized along the x direction.

Figures 7(a)–7(d) show the magnitudes of the TDM $|\boldsymbol{d}_{c0}(\boldsymbol{k})|$ with different internuclear separations, $R = 2a_0, 3a_0, 4a_0, 5a_0$. We can see the clear minima of

$|\boldsymbol{d}_{c0}(\boldsymbol{k})|$ indicated by the arrows. The positions of the minima fit well with Eq. (29). The corresponding harmonic spectra are shown in Figs. 7(e)–7(h). As we can see, there are local minima at the positions predicted by Eqs. (29) and (30) (indicated by the arrows). When $R = ja_0$, the number of minima is equal to $j - 1$. With the increase of R, the number of electrons that can reach the other impurity and participate in the two-center interference decreases, so the local minima in the harmonic spectra gradually become indistinct. As the minima in $|\boldsymbol{d}_{c0}(\boldsymbol{k})|$ get closer, the minima in the harmonic spectra may overlap with each other. We consider the case in which the minima in the harmonic spectra can be clearly observed and choose the internuclear separations around $R = 2a_0$. The harmonic spectra with $R = 1.7a_0, 1.9a_0, 2.2a_0$ are shown in Fig. 8(a). By using Eqs. (29) and (30), we can locate the minima in the harmonic spectra and track the positions of the minima. As we can see in Fig. 8(a), the positions of the minima change with R. Figure 8(b) shows R obtained from the positions of the minima using Eqs. (29) and (30). The blue circles indicate the results with laser intensity $I_1 = 0.36\,\mathrm{TW/cm^2}$. We change the intensity of the driven laser to I_2, so that $\max[A(t)] = 2K_0$, and $I_2 = 1.42\,\mathrm{TW/cm^2}$. The results with laser intensity I_2 are indicated by the red crosses. The obtained R fit the theoretical ones well. The maximum deviation from the theoretical values is 2 Å.

The two-center interference establishes a simple relation between the positions of the minima in the harmonic spectra and the internuclear separation $2R$ of the impurities. This relation may be useful to reconstruct R during the nuclear vibrations of the impurities. In real experiments, only under the condition that the contribution of the highest occupied LES dominates the HHG process can the positions of the minima in the harmonic spectra be determined. This condition can be realized in the donor-doped semiconductors in which the LESs are initially occupied. According to Eqs. (29) and (30), the precision of this reconstruction method is determined
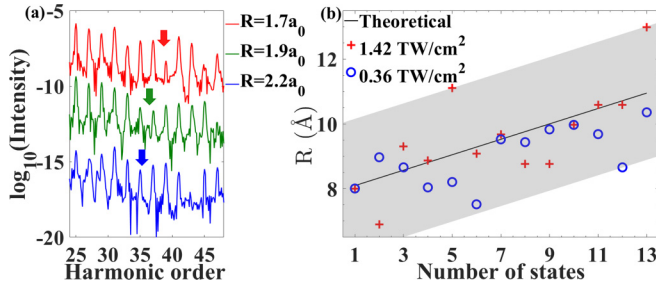
FIG. 8. (a) The parts of the harmonic spectra corresponding to the LEST between the LES and CB states. The results for $R = 1.7a_0$, $1.9a_0$, and $2.2a_0$ are shown. The arrows indicate the minima of the harmonic spectra. (b) The comparison of the theoretical R and R obtained by the positions of the minima using Eqs. (29) and (30). We choose 13 states with internuclear separations around $R = 2a_0$. These states are numbered in ascending order of the internuclear separations. The horizontal coordinate in (b) is the number of states. The black line indicates the theoretical values of R. The blue circles indicate the obtained R with laser intensity $I_1 = 0.36$ TW/cm^2, and the red crosses indicate the results with laser intensity $I_2 = 1.42$ TW/cm^2. The gray shaded area indicates the maximum deviation from the theoretical value is 2 Å.

by the photon energy of the driven laser and the structure of the energy bands. The lower the photon energy is and the wider the energy band is, the higher the precision is. In real experience, an appropriate wavelength of the driven laser should be selected to avoid the undesired laser-induced vibration of atoms and meet the requirement for measurement accuracy. On the one hand, a longer wavelength results in a higher energy resolution and higher precision. On the other hand, the wavelength should not be too long. The time of an optical cycle should be much shorter than the vibrational periods of atoms to make sure the atoms are nearly statical during the HHG process. Additionally, to observe the two-center interference and improve the measurement accuracy in a real experiment, more complex laser fields may be needed.

V. SUMMARY AND CONCLUSIONS

In sparsely doped semiconductors, the breaking of periodic translation invariance in space introduces the NT, and the presence of LESs introduces the LEST. The NT and LEST provide additional transition channels to CB states with various crystal momenta. Our results for a donor-doped semiconductor indicate that considerable electrons can transition to the CB through the additional NT and LEST channels. Therefore, all the harmonics with photon energies greater than 7.3 eV are enhanced. The TDPI pictures further prove that the cutoff extension in the harmonic spectrum is due to the LEST.

We further analyzed the LEST process in a doped semiconductor with a pair of impurities. We found that the LEST is determined by the TDM $\boldsymbol{d}_{c0}(\boldsymbol{k})$, which contains the spatial distribution of the LESs. Furthermore, by examining the characteristics of the TDM $\boldsymbol{d}_{c0}(\boldsymbol{k})$, the idea of two-center interference in doped semiconductors was proposed. Our results indicate that the two-center interference is responsible for the minima in the harmonic spectra. The positions of the minima are related to the internuclear separation between the

impurities. This relation is promising for probing the internuclear separation during the nuclear vibrations on the angstrom scale.

Our work sheds light on the physical mechanisms of the HHG process in doped semiconductors and offers insight into the two-center interference phenomenon. We believe that our results will pave the way for the development of more high-precision and ultrafast measurement methods in the future.

APPENDIX: NUMERICAL DETAILS FOR HIGH-ORDER HARMONIC GENERATION FROM DOPED SEMICONDUCTORS

1. The result in the acceptor-doped semiconductor

The same method is used to investigate the HHG process in the acceptor-doped semiconductors. In Eq. (22), we use
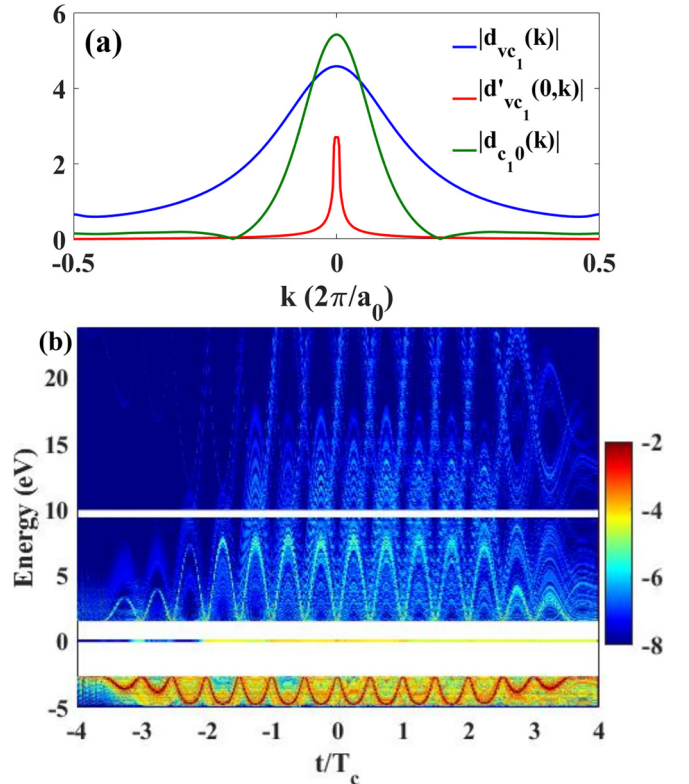

FIG. 9. (a) The TDM of the acceptor-doped semiconductor for the VT, NT, and LEST. The blue curve shows the magnitude of $\boldsymbol{d}_{vc_1}(\boldsymbol{k})$ for VT1, the red curve shows the magnitude of $\boldsymbol{d}'_{vc_1}(0, \boldsymbol{k})$ for the NT, and the green curve shows the magnitude of $\boldsymbol{d}_{c_10}(\boldsymbol{k})$ for LEST1. (b) The TDPI picture for the acceptor-doped semiconductor. The colors indicate the populations of electrons in the VB, LES, CB1, and CB2.
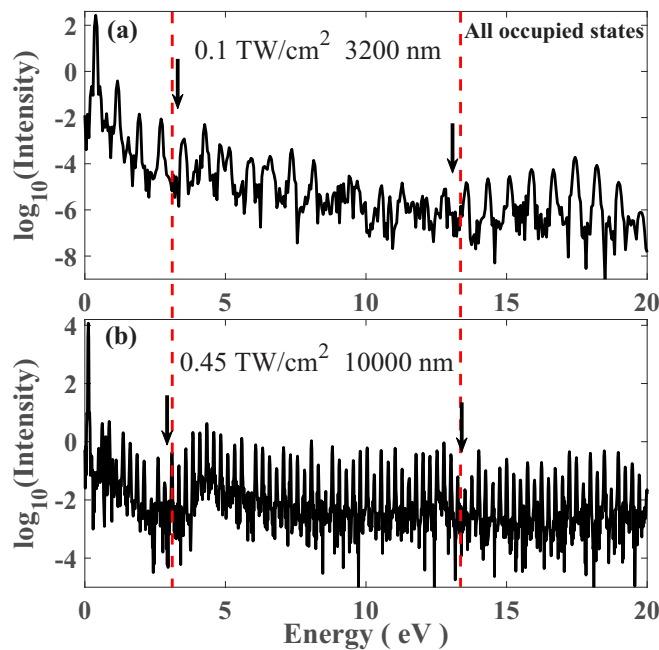
FIG. 10. The harmonic spectra for the doped semiconductor with a pair of impurities. The simulation is performed with all the occupied states in the VB and the LES as the initial state. The intensity and wavelength of the driven laser are shown in the plot. The arrows and dashed lines indicate the minima in the harmonic spectra.

$v_1 = 0.21$ a.u. to model the acceptor-doped semiconductor. All the calculations are performed with the same parameters as described in Sec. III. The band structure for the acceptor-doped semiconductors is the same as in Fig. 1(b), except that the LES is not initially occupied. So the electrons need to transition from the VB states to the LES and then transition to CB states. Figure 9(a) shows the TDM from the VB or LES to CB1, which determines the transitions through the VT, NT, and LEST channels.

For further analysis, the TDPI picture for the acceptor-doped semiconductor is shown in Fig. 9(b). As we can see, there are various electron trajectories in CB1 and CB2, which indicate that the additional NT and LEST channels help electrons get promoted to the CB states with various k.

2. The full calculation for the two-center interference

To show the two-center interference from the odd-parity LES and to address whether the interference can be observed in the full calculation of HHG, we perform a simulation that considers all the occupied states in the VB and the LES as the initial state. The same one-dimensional model as in Sec. III is used to save the time required for the full calculation of HHG. In the model, a pair of impurities is placed at the position $x = \mp 2a_0$. The highest occupied state in this donor-doped semiconductor is an odd-parity LES. The different laser parameters are used to test the robustness of the two-center interference. The other parameters are the same as in Sec. III. The results are shown in Fig. 10; as we can see, the minima caused by the two-center interference are at the positions of 2.9 and 13.3 eV, which are the contributions of the highest occupied odd-parity LES. Therefore, the two-center interference can be observed in the full calculation, and the minima in the harmonic spectra are determined by the highest occupied LES.

[1] P. M. Paul, E. S. Toma, P. Breger, G. Mullot, F. Augé, P. Balcou, H. G. Muller, and P. Agostini, Observation of a train of attosecond pulses from high harmonic generation, Science **292**, 1689 (2001).

[2] M. Hentschel, R. Kienberger, C. Spielmann, G. A. Reider, N. Milosevic, T. Brabec, P. Corkum, U. Heinzmann, M. Drescher, and F. Krausz, Attosecond metrology, Nature (London) **414**, 509 (2001).

[3] F. Krausz and M. Ivanov, Attosecond physics, Rev. Mod. Phys. **81**, 163 (2009).

[4] P. B. Corkum and F. Krausz, Attosecond science, Nat. Phys. **3**, 381 (2007).

[5] J. Li, J. Lu, A. Chew, S. Han, J. Li, Y. Wu, H. Wang, S. Ghimire, and Z. Chang, Attosecond science based on high harmonic generation from gases and solids, Nat. Commun. **11**, 2748 (2020).

[6] L. Li, P. Lan, X. Zhu, and P. Lu, High harmonic generation in solids: Particle and wave perspectives, Rep. Prog. Phys. **86**, 116401 (2023).

[7] S. Ghimire, A. D. DiChiara, E. Sistrunk, P. Agostini, L. F. DiMauro, and D. A. Reis, Observation of high-order harmonic generation in a bulk crystal, Nat. Phys. **7**, 138 (2011).

[8] S. Ghimire and D. A. Reis, High-harmonic generation from solids, Nat. Phys. **15**, 10 (2019).

[9] E. Goulielmakis and T. Brabec, High harmonic generation in condensed matter, Nat. Photon. **16**, 411 (2022).

[10] L. Li, P. Lan, X. Zhu, and P. Lu, Huygens-fresnel picture for high harmonic generation in solids, Phys. Rev. Lett. **127**, 223201 (2021).

[11] L. Li, P. Lan, X. Zhu, T. Huang, Q. Zhang, M. Lein, and P. Lu, Reciprocal-space-trajectory perspective on high-harmonic generation in solids, Phys. Rev. Lett. **122**, 193901 (2019).

[12] G. Vampa, C. R. McDonald, G. Orlando, P. B. Corkum, and T. Brabec, Semiclassical analysis of high harmonic generation in bulk crystals, Phys. Rev. B **91**, 064302 (2015).

[13] G. Vampa, C. R. McDonald, G. Orlando, D. D. Klug, P. B. Corkum, and T. Brabec, Theoretical analysis of high-harmonic generation in solids, Phys. Rev. Lett. **113**, 073901 (2014).

[14] C. Yu, S. Jiang, and R. Lu, High order harmonic generation in solids: A review on recent numerical methods, Adv. Phys.: X **4**, 1562982 (2019).

[15] M. M. S., A. Pattanayak, M. Ivanov, and G. Dixit, Direct numerical observation of real-space recollision in high-order harmonic generation from solids, Phys. Rev. A **100**, 043420 (2019).

[16] A. A. Lanin, E. A. Stepanov, A. B. Fedotov, and A. M. Zheltikov, Mapping the electron band structure by intraband high-harmonic generation in solids, Optica **4**, 516 (2017).

[17] L. Li, P. Lan, L. He, W. Cao, Q. Zhang, and P. Lu, Determination of electron band structure using temporal interferometry, Phys. Rev. Lett. **124**, 157403 (2020).

[18] G. Vampa, T. J. Hammond, N. Thiré, B. E. Schmidt, F. Légaré, C. R. McDonald, T. Brabec, D. D. Klug, and P. B. Corkum, All-optical reconstruction of crystal band structure, Phys. Rev. Lett. **115**, 193603 (2015).

[19] Y. Qiao, Y.-Q. Huo, S.-C. Jiang, Y.-J. Yang, and J.-G. Chen, All-optical reconstruction of three-band transition dipole moments by the crystal harmonic spectrum from a two-color laser pulse, Opt. Express **30**, 9971 (2022).

[20] K. Uchida, V. Pareek, K. Nagai, K. M. Dani, and K. Tanaka, Visualization of two-dimensional transition dipole moment texture in momentum space using high-harmonic generation spectroscopy, Phys. Rev. B **103**, L161406 (2021).

[21] D. Wu, L. Li, Y. Zhan, T. Huang, H. Cui, J. Li, P. Lan, and P. Lu, Determination of transition dipole moments of solids with high-order harmonics driven by multicycle ultrashort pulses, Phys. Rev. A **105**, 063101 (2022).

[22] Y.-T. Zhao, S.-Y. Ma, S.-C. Jiang, Y.-J. Yang, X. Zhao, and J.-G. Chen, All-optical reconstruction of k-dependent transition dipole moment by solid harmonic spectra from ultrashort laser pulses, Opt. Express **27**, 34392 (2019).

[23] H. Lakhotia, H. Y. Kim, M. Zhan, S. Hu, S. Meng, and E. Goulielmakis, Laser picoscopy of valence electrons in solids, Nature (London) **583**, 55 (2020).

[24] Y. S. You, D. A. Reis, and S. Ghimire, Anisotropic high-harmonic generation in bulk crystals, Nat. Phys. **13**, 345 (2017).

[25] Y. S. You, E. Cunningham, D. A. Reis, and S. Ghimire, Probing periodic potential of crystals via strong-field re-scattering, J. Phys. B **51**, 114002 (2018).

[26] S. M. Girvin and K. Yang, *Modern condensed matter physics* (Cambridge University Press, 2019), pp. 198–300

[27] T. Huang, X. Zhu, L. Li, X. Liu, P. Lan, and P. Lu, High-order-harmonic generation of a doped semiconductor, Phys. Rev. A **96**, 043425 (2017).

[28] V. E. Nefedova, S. Fröhlich, F. Navarrete, N. Tancogne-Dejean, D. Franz, A. Hamdou, S. Kaassamani, D. Gauthier, R. Nicolas, G. Jargot, M. Hanna, P. Georges, M. F. Ciappina, U. Thumm, W. Boutu, and H. Merdji, Enhanced extreme ultraviolet high-harmonic generation from chromium-doped magnesium oxide, Appl. Phys. Lett. **118**, 201103 (2021).

[29] C. Yu, K. K. Hansen, and L. B. Madsen, Enhanced high-order harmonic generation in donor-doped band-gap materials, Phys. Rev. A **99**, 013435 (2019).

[30] C. Yu, U. Saalmann, and J. M. Rost, Enhanced high-order harmonics through periodicity breaks: From backscattering to impurity states, Phys. Rev. A **106**, 013105 (2022).

[31] H. Iravani, K. K. Hansen, and L. B. Madsen, Effects of vacancies on high-order harmonic generation in a linear chain with band gap, Phys. Rev. Res. **2**, 013204 (2020).

[32] J. Ma, C. Zhang, H. Cui, Z. Ma, and X. Miao, Theoretical investigation of the electron dynamics in high-order harmonic generation process from the doped periodic potential, Chem. Phys. Lett. **744**, 137207 (2020).

[33] M. S. Mrudul, N. Tancogne-Dejean, A. Rubio, and G. Dixit, High-harmonic generation from spin-polarised defects in solids, npj Comput. Mater. **6**, 10 (2020).

[34] A. Pattanayak, M. M. S., and G. Dixit, Influence of vacancy defects in solid high-order harmonic generation, Phys. Rev. A **101**, 013404 (2020).

[35] C. Yu, K. K. Hansen, and L. B. Madsen, High-order harmonic generation in imperfect crystals, Phys. Rev. A **99**, 063408 (2019).

[36] T.-J. Shao, Laser-field-strength dependence of solid high-order harmonic generation from doped systems, Phys. Rev. A **108**, 023105 (2023).

[37] S. Almalki, A. M. Parks, G. Bart, P. B. Corkum, T. Brabec, and C. R. McDonald, High harmonic generation tomography of impurities in solids: Conceptual analysis, Phys. Rev. B **98**, 144307 (2018).

[38] V.-H. Hoang and A.-T. Le, Factorization of high-order-harmonic-generation yields in impurity-doped materials, Phys. Rev. A **102**, 023112 (2020).

[39] J. L. Krause, K. J. Schafer, and K. C. Kulander, High-order harmonic generation from atoms and ions in the high intensity regime, Phys. Rev. Lett. **68**, 3535 (1992).

[40] P. Corkum, Plasma perspective on strong multiphoton ionization, Phys. Rev. Lett **71**, 1994 (1993).

[41] M. D. Feit, J. Fleck, and A. Steiger, Solution of the Schrödinger equation by a spectral method, J. Comput. Phys. **47**, 412 (1982).

[42] Y. Kosmann-Schwarzbach, The Noether theorems, *The Noether Theorems* (Springer, New York, 2011), pp. 55–64.

[43] J. B. Krieger and G. J. Iafrate, Time evolution of Bloch electrons in a homogeneous electric field, Phys. Rev. B **33**, 5494 (1986).

[44] J. J. Sakurai and E. D. Commins, Modern quantum mechanics, revised edition, Am. J. Phys. **63**, 93(1995).

[45] L. Yue and M. B. Gaarde, Structure gauges and laser gauges for the semiconductor Bloch equations in high-order harmonic generation in solids, Phys. Rev. A **101**, 053411 (2020).

[46] J. C. Slater, A soluble problem in energy bands, Phys. Rev. **87**, 807 (1952).

[47] X. Liu, X. Zhu, P. Lan, X. Zhang, D. Wang, Q. Zhang, and P. Lu, Time-dependent population imaging for high-order-harmonic generation in solids, Phys. Rev. A **95**, 063419 (2017).

[48] J. C. Phillips, Energy-band interpolation scheme based on a pseudopotential, Phys. Rev. **112**, 685 (1958).

[49] M. Lein, N. Hay, R. Velotta, J. P. Marangos, and P. L. Knight, Interference effects in high-order harmonic generation with molecules, Phys. Rev. A **66**, 023805 (2002).

[50] V. V. Serov, I. A. Ivanov, and A. S. Kheifets, Single-photon double ionization of H_2 away from equilibrium: A showcase of two-center electron interference, Phys. Rev. A **86**, 025401 (2012).

[51] C. Vozzi, F. Calegari, E. Benedetti, J.-P. Caumes, G. Sansone, S. Stagira, M. Nisoli, R. Torres, E. Heesel, N. Kajumba *et al.*, Controlling two-center interference in molecular high harmonic generation, Phys. Rev. Lett. **95**, 153902 (2005).

[52] M. Kunitski, N. Eicke, P. Huber, J. Köhler, S. Zeller, J. Voigtsberger, N. Schlott, K. Henrichs, H. Sann, F. Trinter *et al.*, Double-slit photoelectron interference in strong-field ionization of the neon dimer, Nat. Commun. **10**, 1 (2019).

[53] S. Baker, J. Robinson, M. Lein, C. Chirilă, R. Torres, H. Bandulet, D. Comtois, J. Kieffer, D. Villeneuve, J. Tisch *et al.*, Dynamic two-center interference in high-order harmonic generation from molecules with attosecond nuclear motion, Phys. Rev. Lett. **101**, 053901 (2008).

[54] M. Lein, Attosecond probing of vibrational dynamics with high-harmonic generation, Phys. Rev. Lett. **94**, 053004 (2005).